Structural study on the architecture of the bacterial ATP synthase F_o motor

Jonna K. Hakulinen[a], Adriana L. Klyszejko[a], Jan Hoffmann[b], Luise Eckhardt-Strelau[a], Bernd Brutschy[b,c], Janet Vonck[a,1], and Thomas Meier[a,c,1]

[a]Department of Structural Biology, Max Planck Institute of Biophysics, 60438 Frankfurt/Main, Germany; and [b]Institute of Physical and Theoretical Chemistry, and [c]Cluster of Excellence Macromolecular Complexes, Goethe University, 60438 Frankfurt/Main, Germany

Edited by John E. Walker, Medical Research Council Mitochondrial Biology Unit, University of Cambridge, Cambridge, United Kingdom, and approved June 5, 2012 (received for review March 7, 2012)

We purified the F_o complex from the *Ilyobacter tartaricus* Na^+-translocating F_1F_o-ATP synthase and performed a biochemical and structural study. Laser-induced liquid bead ion desorption MS analysis demonstrates that all three subunits of the isolated F_o complex were present and in native stoichiometry (ab_2c_{11}). Cryo-electron microscopy of 2D crystals yielded a projection map at a resolution of 7.0 Å showing electron densities from the c_{11} rotor ring and up to seven adjacent helices. A bundle of four helices belongs to the stator a-subunit and is in contact with c_{11}. A fifth helix adjacent to the four-helix bundle interacts very closely with a c-subunit helix, which slightly shifts its position toward the ring center. Atomic force microscopy confirms the presence of the F_o stator, and a height profile reveals that it protrudes less from the membrane than c_{11}. The data limit the dimensions of the subunit a/c-ring interface: Three helices from the stator region are in contact with three c_{11} helices. The location and distances of the stator helices impose spatial restrictions on the bacterial F_o complex.

bioenergetics | membrane protein complex | 2D crystallization | ion translocation mechanism | membrane F_o rotor-stator

F-type ATP synthases are the major supplier of chemically bound energy in the form of ATP in all living cells. These enzymes use a transmembrane electrochemical ion gradient as an energy source to convert ADP and P_i to ATP. Two structurally and functionally distinct domains together form a macromolecular protein complex: the water-soluble F_1 complex (1), with a subunit stoichiometry of $\alpha_3\beta_3\gamma\delta\varepsilon$, and the membrane-embedded F_o complex (2) (ab_2c_{8-15}). Both complexes can function as separate and independent rotary motors, fueled by either H^+ or Na^+ (F_o) or ATP (F_1). Structurally, they are connected by a static peripheral (δb_2) and a rotating central ($\gamma\varepsilon$) stalk. Ion translocation through the F_o complex induces torque, which leads to rotation (3, 4) of the enzyme's rotor ($\gamma\varepsilon c_n$). The central stalk γ-subunit rotates inside the F_1 $(\alpha\beta)_3$ headpiece and elicits sequential conformational changes in the three catalytic β-subunits, finally leading to ATP synthesis (5). In the reverse direction, along the same operation principle, the enzyme can act as an ATP hydrolysis-driven ion pump (6, 7).

The mechanism of ion translocation and torque generation in the F_o complex involves the stator subunits a and b_2, as well as the rotor ring (c_n, c-ring). In bacteria, the outer stalk consists of a pair of b-subunits, each forming a long, membrane-penetrating, and amphiphilic α-helix, which is in contact with the α-, β-, and δ-subunits at the F_1 headpiece of the enzyme, and with the a-subunit and the c-ring in the membrane (8–10). Its coiled and stiff construction was proposed to make it act as a physical barrier against the F_o-generated torque (11, 12), but the b-subunit might also be involved in the ion translocation process itself (13, 14).

Several c-ring structures (and 1 K-ring from V-type ATPase) were solved by X-ray crystallography at high resolution and with unequivocal side-chain assignments (15–19). The synergistic picture that arises from the available c-ring structures poses functional restrictions but also suggests a conserved mechanism in rotary ATPases (20, 21). Thus, at least as regards the c-ring, an overall model for ion translocation has started to develop in the past few years.

The exact role of the stator a-subunit, however, remains unclear because structural information for this subunit is scarce. The *Escherichia coli* a-subunit is generally accepted to consist of five transmembrane α-helices (9, 22). It contains a conserved region at the predicted helix 4, including an arginine residue that has been shown to be essential for function (23–25). In addition to the models for the a-subunit derived from a large number of cross-linking and aqueous accessibility studies (9, 26–29), a sub-nanometer resolution structure of the V-type ATP synthase from the bacterium *Thermus thermophilus* has been reported recently (30). This cornerstone contribution suggests that the membrane stator complex of this rotary ATPase consists of eight transmembrane helices, forming two bundles of four helices each. Each bundle is in contact with different c-subunits and forms a half channel that provides ion access from either the periplasm (entrance pathway) or cytoplasm (exit pathway). These structural data appear fully in agreement with a previously proposed model of F_o function (3), as well as an F_o-mechanistic proposal based on high-resolution X-ray data of the c-ring (20). However, there are currently no structural data available for the rotor-stator interface (c-ring/a-subunit) in F-type ATP synthases. Clearly, structural data on the molecular architecture of the bacterial F_o stator are essential for a better understanding of the F_o operation mechanism.

We performed a study on the F_o complex from the bacterium *Ilyobacter tartaricus*. The isolated F_o complex was in native stoichiometry, and it was suitable as a target for biochemical and structural investigations. A projection map obtained from EM of 2D crystals at a resolution of 7.0 Å shows electron densities next to the c_{11} rings. They belong to the stator a-subunit, and perhaps the b-subunit, and are also visible on atomic force microscopy (AFM) topographic images. On the basis of these observations, we propose a model for the localization and arrangement of the bacterial F_o stator subunits at the c-ring and discuss an ion translocation model, including the data presently available in the literature.

Author contributions: T.M. designed research; J.K.H., A.L.K., J.H., L.E.-S., J.V., and T.M. performed research; J.K.H. developed the F_o purification protocol used in this work and crystallized the F_o complex; B.B. contributed new reagents/analytic tools; J.K.H., A.L.K., J.H., J.V., and T.M. analyzed data; J.K.H., A.L.K., J.V., and T.M. wrote the paper.

The authors declare no conflict of interest.

This article is a PNAS Direct Submission.

Freely available online through the PNAS open access option.

[1]To whom correspondence may be addressed. E-mail: janet.vonck@biophys.mpg.de or thomas.meier@biophys.mpg.de.

See Author Summary on page 11908 (volume 109, number 30).

This article contains supporting information online at www.pnas.org/lookup/suppl/doi:10.1073/pnas.1203971109/-/DCSupplemental.

Results

Purification of the *I. tartaricus* F_o Complex. We developed a purification protocol of the *I. tartaricus* F_o complex [ITF_o (ab_2c_{11})] in amounts suitable for 2D crystallization experiments. An expression system was used that allows the production of His-tagged *I. tartaricus* F_1F_o-ATP synthase (ITF_1F_o) in *E. coli* DK8 cells. To purify ITF_o, we stripped off the F_1 complex using urea. Finally, a highly pure ITF_o was obtained by metal chelate affinity chromatography (Fig. 1*A*). Using the same expression plasmid, we also purified ITF_1F_o to compare it with the purified ITF_o (Fig. 1*A*). The final ATPase activity was 8.8 U/mg, and both protein subunits a and b, as well as the c_{11} ring, showed an identical migration pattern. Silver stain signals on the SDS gel indicated that all F_o subunits were intact and apparently also kept in the expected stoichiometric amounts during the isolation procedure. The isolated ITF_o was further analyzed by size exclusion chromatography, resulting in an ITF_o-containing peak (e.g., in the presence of 0.5% Cymal-5) (Fig. S1). The a-subunit in isolated F_o showed a single signal on the Western blot, indicating that the a-subunit was intact and not degraded during purification (Fig. 1*A*). The final yield of pure F_o complex varied significantly from preparation to preparation and was in the range of 0.4–1.5 mg per 6-L × 2-L shaker culture setup.

Laser-Induced Liquid Bead Ion Desorption MS of the Purified ITF_o. Laser-induced liquid bead ion desorption (LILBID) MS allows one to analyze masses and stoichiometries of macromolecular membrane protein complexes in detergent solution at physiological buffer conditions. The method has a proven track record to be applicable on, for example, ATP synthases (31), as well as their c-rings (32). We therefore analyzed the assembly and stoichiometry of the isolated ITF_1F_o and ITF_o by LILBID-MS and compared the results with the ITF_1F_o, which we isolated from WT *I. tartaricus* cells (Fig. 1*B* and Fig. S2). All theoretically calculated and measured masses from this experiment are summarized in Table S1. At soft laser intensity, the WT and heterologously expressed ITF_1F_o both showed a mass of 548 ± 5 kDa for the complete F_1F_o complex. At high laser intensity, all eight structural ATP synthase subunits were identified in the spectra; all measured masses corresponded with the expected masses for both ITF_1F_o complexes. The purified ITF_o analyzed at soft laser intensity shows, in addition to higher charged peaks (2− to 5−), the singly charged peak of the F_o complex at 168 ± 2 kDa, corresponding exactly to the calculated mass of the ab_2c_{11} complex. At high laser intensity, the ITF_o dissociated into protein subunits a-His_{12} (34 ± 0.3 kDa), c (8.8 ± 0.1 kDa), and b (18.6 ± 0.2 kDa), also in agreement with the literature values. Further, several oligomers were detected in the mass spectra (c_2, c_3, c_4, and c_1b_1). Taken together, LILBID-MS showed that the measured masses of the complexes (WT ITF_1F_o, recombinant ITF_1F_o, and ITF_o) correlate well with the calculated masses. Hence, the purified protein complexes show a native subunit composition and stoichiometry: $\alpha_3\beta_3\gamma\delta\varepsilon ab_2c_{11}$ for ITF_1F_o and ab_2c_{11} for ITF_o.

EM Analysis of Reconstituted and 2D Crystalline ITF_o. The ITF_o was subjected to several 2D crystallization attempts, in which the various parameters, such as the protein concentration, lipid type, lipid-to-protein ratio (LPR), pH, dialysis time and temperature, and salt conditions, were tested. The samples were screened by EM (*SI Results* and Figs. S1 and S3 provide more information about ITF_o stability and lipid analysis, respectively). Vesicles with tightly packed proteins but no 2D crystals were found. Some samples containing densely reconstituted protein were tested by immunogold labeling, and the presence of the a-subunit was confirmed at pH 8.0 and 8.5 (Fig. 2 *A* and *B*), whereas in control experiments with empty vesicles or reconstituted c_{11} rings only, no gold particles were found (Fig. 2 *C* and *D*).

Separation of the rotor and stator components in the F_o part during crystallization procedures of ATP synthase is a known feature of the enzyme (e.g., it also occurred in 3D crystallization trials of the yeast mitochondrial ATP synthase, yielding F_1c_{10} subcomplexes) (33). Similarly, the inherent tendency of *I. tartaricus* c_{11} rings to form 2D crystals hampered us in the crystallization of the entire ITF_o; in some cases, 2D crystals of c_{11} rings in the previously described space group *p*1 (34–36) appeared. However, under some conditions, 2D crystals in plane group $p12_1$ were formed. This crystal form was observed when reconstituting ITF_o in a 1-palmitoyl-2-oleoyl-*sn*-glycero-3-phosphocholine (POPC)/1-palmitoyl-2-oleoyl-*sn*-glycero-3-phospho-(1′-rac-glycerol) (POPG)/1-palmitoyl-2-oleoyl-*sn*-glycero-3-phosphoethanolamine (POPE) mixture at an LPR of 0.94–1.25 (protein concentrations from 0.95-1.5 mg/ml) at 20–25 °C and with a pH of 8.0 and 150–250 mM KCl. These crystalline areas, however, were scarce and were parts of small sheets with a size of ∼0.3–0.6 μm (Fig. 2*E*).

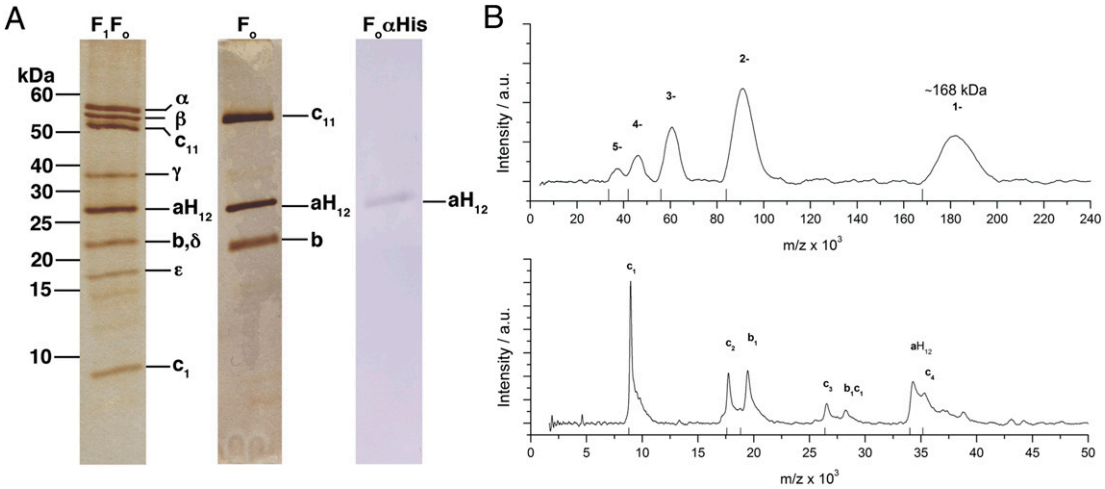

Fig. 1. Purification and MS analysis of the ITF_o. (*A*) Silver-stained SDS/PAGE (13.1%) with purified ITF_1F_o and ITF_o. Western blot of purified ITF_o against anti–a-His_{12} (aH_{12}). The molecular masses (kDa) and F_1F_o protein subunits are indicated. (*B*) LILBID-MS of the ITF_o. At low laser intensity (*Upper*), a single charged (1−) peak of ITF_o has a mass of 168 kDa. At high laser intensity (*Lower*), the ITF_o was completely dissociated into single subunits (aH_{12}, b_1, and c_1) and to various ITF_o subunit oligomers (c_2, c_3, c_4, and c_1b_1).

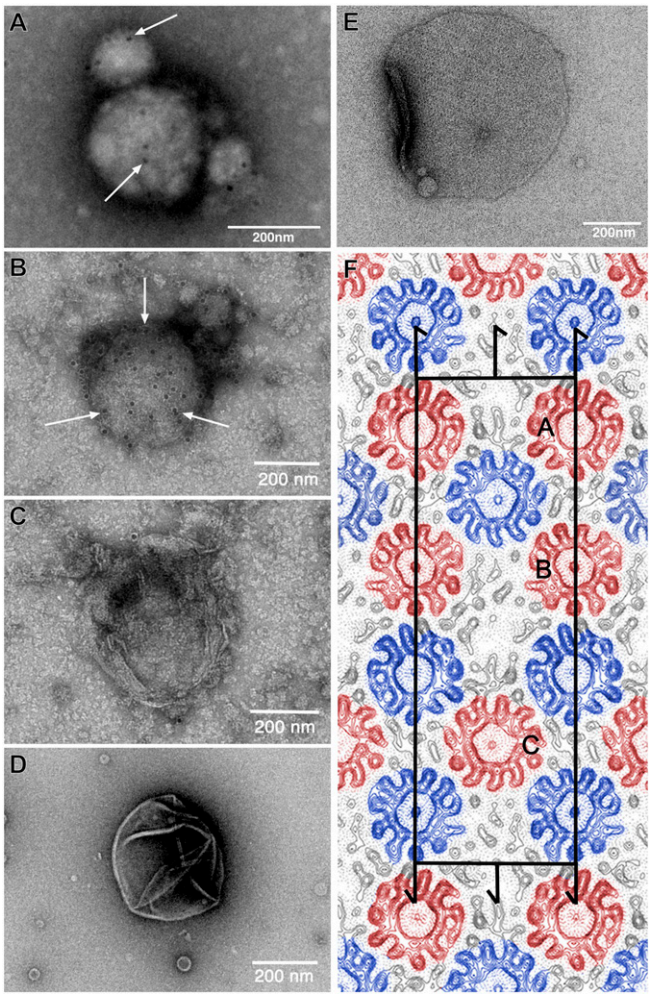

Fig. 2. Two-dimensional crystallization and EM analysis of the ITF_o. ITF_o purified in dodecyl maltoside was reconstituted for 2D crystallization at an LPR of 1.2 and a protein concentration of 1.1 mg/mL. To investigate whether the His-tagged a-subunit is present in the samples, immunogold labeling was performed. Electron micrographs of an immunogold-labeled (anti–a-His_{12}, arrows) vesicle from reconstituted ITF_o at pH 8.0 (*A*) and pH 8.5 (*B*) are shown. As a dialysis buffer, we used 50 mM Tris·HCl (at both pHs), 120–150 mM KCl, 3 mM NaN_3, and 1 mM DTT. The samples were dialyzed at 4 °C. As controls, we used empty lipids at pH 8.5 (*C*) and reconstituted c_{11} proteoliposomes (*D*) as done in the study by Pogoryelov et al. (20), which did not show any bound gold label. (*E*) Electron micrograph of a negatively stained $p12_1$ 2D crystal from ITF_o crystallization setup. (*F*) Projection map at a resolution of 7.0 Å with symmetry $p12_1$ applied. Continuous lines represent density above the mean, and dotted lines represent negative contours. The rectangular unit cell is shown with a = 252 Å and b = 81 Å. Screw axes parallel to the membrane plane are indicated. One unit cell contains two asymmetrical units with three c_{11} rings in each (marked as A, B, and C); oppositely oriented c_{11} rings are indicated in red and blue. Densities of F_o stator subunits are visible in the map adjacent to c_{11} rings (black).

From cryoelectron micrographs of crystals embedded in trehalose, structure factors up to 5 Å were obtained after correction for lattice distortions (Fig. S4). The five best lattices were merged to 7.0 Å (Fig. S5) to calculate a projection electron density map (Fig. 2*F*). The rectangular unit cell has the cell dimensions a = 252 Å and b = 81 Å. One unit cell contains two asymmetrical units with three c_{11} rings in each. The c_{11} rings are present in an alternating "up" and "down" orientation, as also observed in the crystals of plane group $p1$. In both plane groups, each ring establishes crystal contacts with neighboring rings oriented in opposite cytoplasmic/periplasmic directions. Strikingly, however, the $p12_1$ crystal maps showed, in addition to the c-ring densities, unique prominent densities that were not present in any of the previously obtained *I. tartaricus* c_{11} projection maps (34–36). They were located in the proximity of the c-rings at three different positions in the asymmetrical unit. These three densities build irregular structures in proximity to two, three, or four rings (Figs. S6 and S7). The unique features are partly resolved into strong density peaks that may represent transmembrane helices, perpendicular to the membrane. Up to seven helices may be present in total, but their appearance is ambiguous in some cases.

AFM. Two-dimensional crystalline ITF_o samples were investigated by high-resolution AFM (Fig. 3). Two different packings were observed. The $p1$ crystals, as seen also in c-ring crystals (34), were the most abundant (Fig. 3*A*). The c_{11} rings showed two orientations, either visible from the periplasmic side and filled with phospholipids (37) or visible from the cytoplasmic side with no central mass inside (Fig. 3 *A*, *D*, and *E*). In some of the topographs, the crystalline areas showed a different packing, in which one ring was in contact with four neighboring rings oppositely oriented in the membrane. Despite an intensive search, 2D crystals of the $p12_1$ packing type were not found.

In regions of densely packed protein, close to the 2D crystal borders, c_{11} rings with and without a central plug were visible. The latter were better resolved (Fig. 3 *A* and *C*), and a height profile analysis performed on cross-sections of selected regions in the topographs (Fig. S8) revealed that they protruded 0.7 ± 0.1 nm (n = 20) from the membrane surface level. Interestingly, between two neighboring c-rings, additional objects sometimes could be seen (Fig. 3*B*, white arrows). They protruded only 0.4 ± 0.1 nm (n = 23) from the membrane. Each protrusion most likely represents an attached a-subunit with an average width and length of 1.5 ± 0.3 nm (n = 21). Based on the height difference in the unprocessed AFM topographs, these objects could be distinguished from c_1 (38) or c_n oligomers occasionally attached at the outside of the c-rings (Fig. 3*B*, red arrows). The presence or absence of the b-subunit could not be determined with certainty. However, in addition to the described densities, highly flexible parts protruding higher than the c-rings and presumably belonging to the b-subunit were present in the samples, but these caused artifacts during imaging.

Noncrystallographic Symmetry Averaging of the ITF_o. To investigate whether there are conserved elements in the three extra densities of the asymmetrical unit of the $p12_1$ crystals, noncrystallographic symmetry (NCS) averaging based on single-particle averaging was performed. The three c_{11} rings in the asymmetrical unit with the same up/down orientation and the extra densities next to them were averaged using translational and rotational alignment in IMAGIC (39). Because it was not clear which extra density belongs to which ring, all six possibilities were taken into consideration (Fig. S6). A single ring with all surrounding densities was contoured, excluding the neighboring rings (Fig. S7 *A–C*), and then aligned and averaged with the two others (Fig. S7 *D–I*). In all six possible arrangements, the c-ring densities were enhanced by the alignment, but only in one were the extra densities significantly increased relative to the background (Fig. S7*D*). The selected regions are shown in Fig. 4 *A–C*. Each of the extra densities contains a four-helix bundle (red in Fig. 4). In the average (Fig. 4*D*) of the selected three regions, the four-helix bundle can also be seen, although one helix is very weak because of a slight difference in its position within the three regions. Two of these four helices interact with one or two outer α-helices from the c_{11} ring. The distances measured between the highest density peaks of the extra densities and the c_{11} peaks are shown in Fig. 4*E* (lines *a–g*). Apart from the four-helix bundle, only 11.4 ± 0 Å apart, a fifth prominent helix (brown in Fig. 4) interacts with two

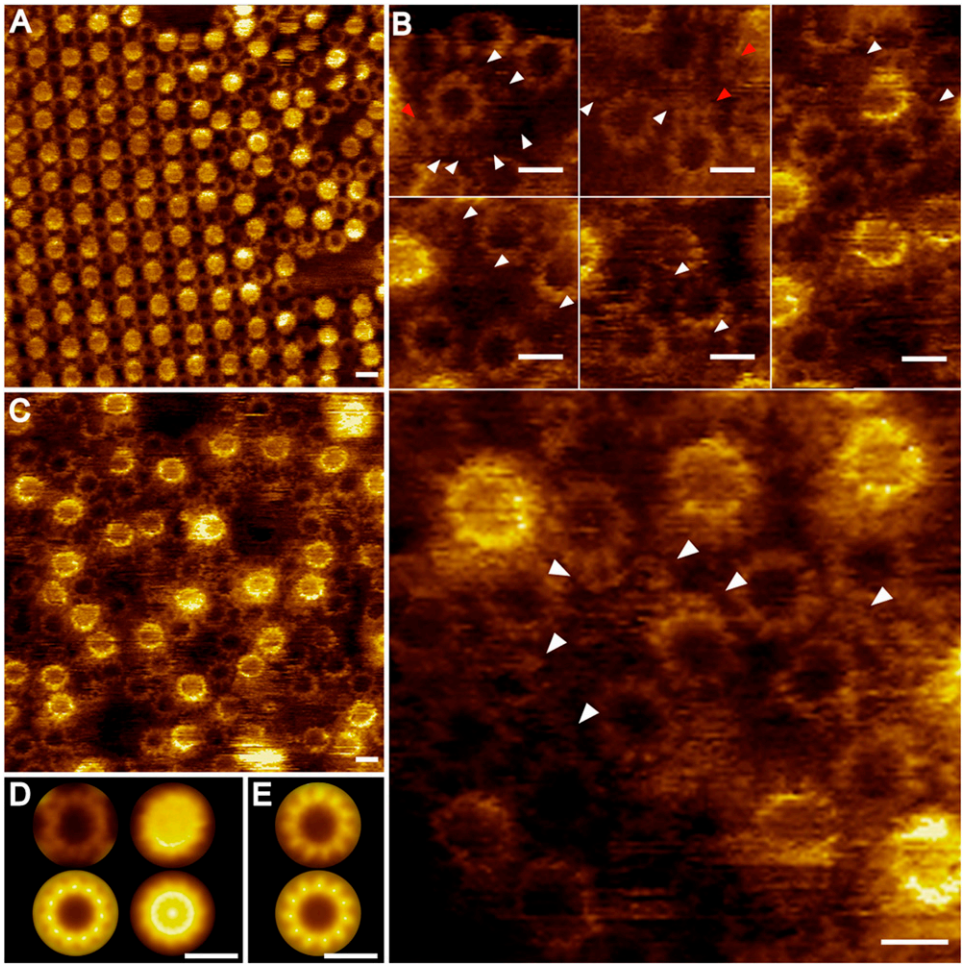

Fig. 3. AFM images of reconstituted ITF_o samples. A crystal composed of c_{11} rings (*A*) and paracrystalline arrays of reconstituted ITF_o with visible c_{11} rings (*C*) are shown. (*B*) Gallery shows the presence of additional densities between the c_{11} rings (white arrowheads) and broken c-rings (red arrowheads). (*D*) Averages of the cytoplasmic (*Left*; $n = 100$) and periplasmic (*Right*; $n = 50$) interfaces of c_{11} from the crystals: nonsymmetrized (*Upper*) and symmetrized (*Lower*). (*E*) Average of the c_{11} rings from the paracrystalline arrays (*Upper*; $n = 100$) and their symmetrization (*Lower*). (Scale bars: *A* and *C*, 10 nm; *B*, 5 nm; *D* and *E*, 3 nm.)

adjacent outer c_{11} ring helices (nos. 1 and 11 in Fig. 4*E*) at a very close distance, 10.6 ± 1.8 Å and 9.5 ± 1.7 Å, respectively. The packing in this region (*g*) is so tight that the density center of helix no. 11 seems to shift toward the c-ring center by a few angstroms (Fig. 4*E*, red line). It is not clear whether this shift is induced by the various ITF_o crystal contacts or represents a native conformation of the protein complex. Further, up to two more helices are present at each position in the asymmetrical unit. Two prominent helices are visible in Fig. 4 *B* and *C* next to the bundle (blue in Fig. 4), in a position that is occupied by a neighboring c-ring in Fig. 4*A*. It is thus possible that the densities in Fig. 4*A* are in a different conformation than the other two because of crystal contacts. In pairwise averaging (Fig. S7 *J–L*), it can be seen that the extra densities in Fig. 4 *B* and *C* are most similar to each other. The interaction of the c-ring and the neighboring density covers a length of ~21 Å and involves three α-helices of the c-ring and up to three α-helices of the stator.

Discussion

This work provides structural data of the stator components of the F_o complex from a bacterial F-type Na^+-ATP synthase at a resolution of 7.0 Å. The map shows electron densities that can be unequivocally attributed to the 22 α-helices of the *I. tartaricus* c_{11} ring. In addition, up to seven electron density peaks are visible next to the c-rings. These must represent the transmembrane domains of the F_o stator components, namely, the a-subunit and perhaps also the b-subunit. The presence of the b-subunit could not be explicitly confirmed. These densities were weaker than the helix densities of the c-rings, which may mean that the helices of the stator are shorter or more highly tilted than the c-ring helices, or that the stator components are present at a lower occupancy in the crystal. AFM studies showed that these features protrude less from the membrane than the c-rings. LILBID-MS analysis, gel filtration, and electrophoresis experiments show that all F_o subunits were present and in native stoichiometry (ab_2c_{11}) before the 2D crystallization setups were made. It is, however, possible that some of the stator components dissociate during the crystallization process and that they are present only in the noncrystalline parts of the vesicles.

Electron Density Map Interpretation. A remarkable feature of the map is the presence of a four-helix bundle (red in Fig. 4). The distances between pairs of helices in this bundle are almost equal (10.1 ± 1.5 Å), and two of those helices contact the c-ring. Concurrent with our data, a four-helix bundle has been proposed for the *E. coli* a-subunit (40). Two four-helix bundles are also visible in the membrane-embedded stator region of the *T. thermophilus* ATP synthase, as recently visualized by cryo-EM (30). Our data hence suggest that such bundles are conserved elements of the stator a-subunits, and thus important for F_o stator

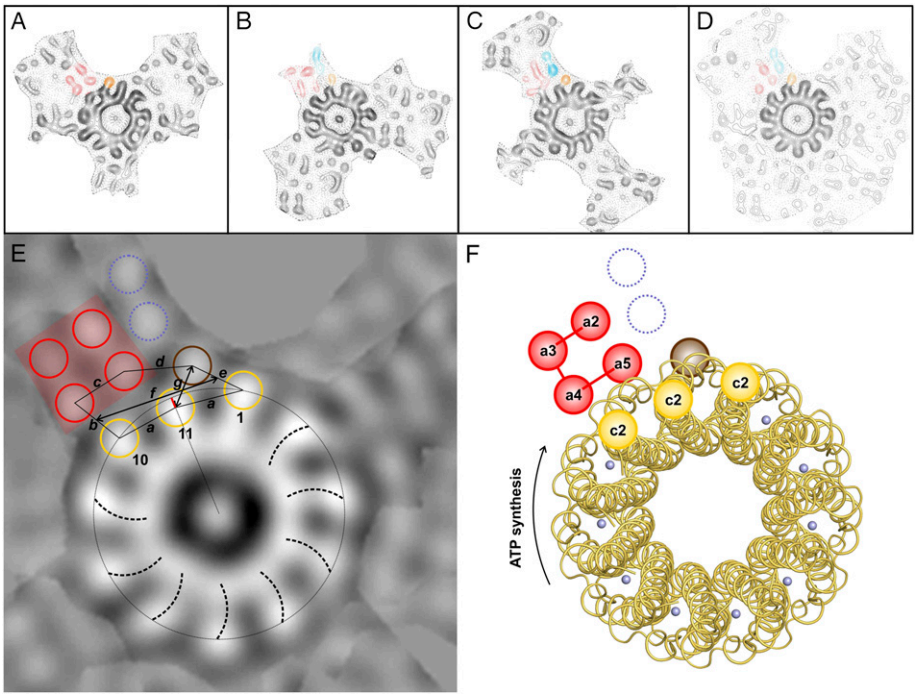

Fig. 4. NCS averaging, ITF_o map, and model interpretation. (*A–C*) Three selected c-rings with their adjacent regions derived from the projection map (Fig. 2*F*) were cut out and aligned to each other. Ring B was rotated 33.9°, and ring C was rotated 32.9° counterclockwise relative to ring A. (*D*) Average of *A–C*. Densities that are present in all three positions are indicated with red and brown colors; two densities only seen in *B* and *C* are shown in blue. (*E*) Map interpretation using conserved densities and distance determination. Outer helices from c_{11} that make contact with the extra densities (1, 10, and 11) are circled in yellow. One density (11) is not in c_{11}-symmetrical position; a red line indicates the shift. Densities outside c_{11} are circled in red (four-helix bundle), blue, and brown. The vorticity of the rings is visible and shows that the view (here and red rings in Fig. 2) is from the periplasm (35). A network of helix-to-helix distances (measured between the highest density peaks) is indicated: $a = 11.5 \pm 0.8$ Å, $b = 10.5 \pm 0.8$ Å, $c = 10.1 \pm 1.5$ Å, $d = 11.4 \pm 0$ Å, $e = 10.6 \pm 1.8$ Å, and $g = 9.5 \pm 1.7$ Å. The subunit a/c-ring interface has a length of ~21 Å (*f*); it involves three helices from the stator (a-subunit and possibly b-subunit) and maximally three α-subunits of the c_{11} ring. (*F*) Model interpretation. According to the model for the *E. coli* a-subunit, the four-helix bundle consists of helices a2–a5. The other densities could represent the b-subunit, a0, or a1. The possible helix assignment of the four-helix bundle is indicated. Cytoplasmic and periplasmic connections are indicated as in Fig. S9*C*. The color code and view are the same as in *E*. Rotation of the c-ring in the ATP synthesis direction is indicated by an arrow. The blue spheres represent Na^+ on the c_{11} ion binding site.

function. At the side of the bundle, a fifth helix is in close contact with the c-ring (brown in Fig. 4). The map indicates that this rotor-stator helix arrangement is packed so tightly that the usual symmetry of the c-ring apparently is disturbed at this position and one of the outer helices (no. 11 in Fig. 4) shifts slightly inward. This remarkable observation might have consequences for the F_o mechanism because it could indicate functionally important conformational changes that can occur during the ion exchange process. However, this helix is involved in crystal contacts; any mechanistic interpretation needs further careful structural investigation.

In addition to these five helices, there are up to two more density peaks present, but their position differs depending on the reference ring. In two cases (blue in Fig. 4 *B* and *C*), there are two peaks between the four-helix bundle and a c-ring in close proximity to the fifth helix. In one case (Fig. 4*A*), a neighboring c-ring occupies this position, but two helices are visible at the side of the four-helix bundle facing away from the c-ring and the fifth helix. Apparently, the c-rings are more rigid than the densities next to them, and the stator subunits might be only weakly bound to the c-ring. Therefore, some of the stator helices perhaps adopt a conformation that simply fits best in the crystal lattice. The inherent flexibility of the rotor-stator region remains a pertinent problem for structural investigations. A covalent linking of the rotor with the stator (25) seems a valid approach for future studies with a stabilized F_o complex.

The interpretation of the map shows that the rotor-stator interface harbors three stator transmembrane helices, which are in contact with three outer (C-terminal) c_{11} ring helices over a length of ~21 Å. Although our data suggest that the visible helices are rather straight, a limitation of the projection map is that their 3D path cannot be seen. In the V-type ATP synthase, there are indications (30) that some a-subunit helices approach the ion binding site in the middle of the membrane, at the narrowest part of the hour glass-shaped c_{11} ring (15, 35).

Helix Assignment. A secondary structure and topography analysis of the *I. tartaricus* a-subunit suggests six α-helices (*SI Results* and Fig. S9), but a complicating factor for the helix assignment in our map was the presence or absence of the b-subunit(s) after 2D crystallization. Cross-link experiments performed with the ITF_1F_o based on the *E. coli* and *I. tartaricus* enzymes (26, 27) show that helix a4, harboring the functionally important a-subunit arginine (25), and helix a5 (41) are in contact with outer c-ring helices (c2). Biochemical studies proposed that the helices a2–a5 in *E. coli* form a four-helix bundle (40). There is also evidence that both b-subunit helices can interact with the same c-monomer (10) and two a-subunit loop regions (a1–a2 and a2–a3) can be cross-linked to the b-subunit (9), suggesting the close proximity of helix a2 to the N-terminal part of the b-subunit. The four-helix bundle (red in Fig. 4) could therefore represent helices a2–a5. The assignment of the fifth density (brown in Fig. 4) as well as the two remaining densities (dashed blue lines in Fig. 4*F*), which are missing in one of the three densities (Fig. 4*A*), is less clear. They all could represent one or two b-subunits as well as one or both a-subunit helices (a0, a1). It is also possible that as a result of crystal

contacts, some of the density in Fig. 4*A* results from a different conformation than the density observed in Fig. 4 *B* and *C*.

Ion Translocation. An ion translocation model through the F_o complex involves two ion pathways, which both end at the ion binding site of the c-ring in the middle of the membrane (3). The two pathways have been proposed to be physically separated by the conserved arginine in the a-subunit with a dual role: (*i*) acting as an electrostatic separator between the two access/release pathways (25) and (*ii*) catalyzing reversible ion exchange at the rotor's (c-ring) ion binding site (15, 20). A bundle of four or sometimes three helices was observed in ion (H^+ and Na^+) conducting membrane proteins as sufficient to provide a functional ion conducting pathway (42, 43). Our data show that the bacterial F_o stator component has one four-helix bundle and, in addition, up to three more helices that belong to the a-subunit or perhaps to the b-subunit. They clearly do not form a second helix bundle, but they can still be involved in ion translocation. Apparently, despite a conserved ion translocation mechanism in different rotary ATPase types (20, 21), the rotor-stator interface architecture varies and involves two four-helix bundles in a V-type ATPase (30) instead of one, as seen here.

A total number of eight (*I. tartaricus*) or seven (*E. coli* and most other bacteria) (Fig. S9) helices are, in principle, compatible with the requirement of three to four helices per ion pathway. Although our data do not yet allow interpretations about the locations of these access and exit ion pathways, they appear to be compatible with the contemporary model of ion translocation (20). A feature of this model is, for example, that the F_o stator region provides a hydrated region in which the ion binding glutamate of the c-ring can change its conformation from locked to open, enabling ion exchange. The rotor-stator interface we found is large enough to provide such an environment; our work imposes previously undescribed spatial restrictions on the F_o complex in bacterial ATP synthases.

Materials and Methods

Expression and Purification of ITF_1F_o and the F_o Subcomplex. ITF_1F_o and ITF_o were expressed and purified as described in detail in *SI Materials and Methods*. Briefly, for ITF_o purification, the membranes were washed with 3.5 M urea before solubilization to separate F_1 from F_o; subsequently, ITF_o was purified via affinity chromatography.

Two-Dimensional Crystallization of ITF_o. Lipids were dissolved in 1% decyl-β-D-maltoside at 4 mg/mL. ITF_o purified in dodecyl-β-D-maltoside was mixed with POPC, POPE, and POPG (1:1:1 mixture) at a protein concentration of 0.95–1.5 mg/mL and at LPRs of 1–1.25 (wt/wt) and incubated at 4 °C overnight. The samples were dialyzed in dialysis buttons (Hampton Research) against 50 mM Tris·HCl at pH 8.0, 150–250 mM KCl, 3 mM NaN_3, and 1 mM DTT. The crystals in plane group $p12_1$ formed at 20 °C to 25 °C after 8 wk of dialysis.

EM, AFM, and LILBID-MS. Negatively stained samples [1.5% (wt/vol), uranyl acetate] were screened using a Philips CM120 microscope at a magnification of 45,000×. Samples containing crystals were frozen by the back-injection method in 4.5% (wt/vol) trehalose on carbon-coated copper grids, and data collection was as described by Matthies et al. (44). Images were processed using the software 2dx (45) to correct lattice distortions and the contrast transfer function (46). Five lattices were merged using the CCP4 suite (47) to a resolution of 7.0 Å to generate a projection map. An isotropic temperature factor (B = −200 $Å^2$) was applied to compensate for the resolution-dependent degradation of image amplitudes. Immunogold on grid labeling, AFM of reconstituted ITF_o, and LILBID-MS were performed as described in *SI Materials and Methods*.

NCS Averaging. Real-space NCS averaging of the c_{11} rings and extra densities was performed using IMAGIC (39). An image was created of each of the three rings in the asymmetrical unit in the same in-plane orientation with its surrounding densities. The other rings were masked out manually. Six possible arrangements of rings with associated extra density were identified. The rings were prealigned to superimpose the extra densities for each possible arrangement. Then, the 11 subunits of the rings were accurately aligned translationally and rotationally. The aligned images were averaged, and the averages were examined for enhanced densities outside the rings. This was the case for only one of the six possibilities.

ACKNOWLEDGMENTS. We thank Anke Terwisscha van Scheltinga for help with the initial NCS averaging. Plasmid pItTr5His was a kind gift from Peter Dimroth's laboratory (cloned: Benjamin Oberfeld, His-tag: Christoph von Ballmoos). J.K.H. thanks Deryck Mills for the help with microscopy. We thank Friederike Joos for the help with the immunogold labeling. T.M. thanks John Rubinstein for providing his manuscript and structure data prior to publication of the study by Lau and Rubenstein (30). Werner Kühlbrandt is also thanked for his generous support of T.M.'s research. We also thank Daniel J. Müller for help in AFM and reading the manuscript, Petra Schwille (Biotechnology Center, Dresden University of Technology, Dresden, Germany) for providing laboratory space and support at Dresden University of Technology to perform the AFM experiments, and José Faraldo-Gómez for useful comments on the manuscript. T.M. was financially supported (position for J.K.H. and materials) by the Collaborative Research Center 807 of the German Research Foundation. Further financial support (materials) for this project was provided to T.M. and B.B. by the Cluster of Excellence "Macromolecular Complexes" at the Goethe University Frankfurt (Project EXC 115) and the EuroSYNBIO-Nanocell project of the European Science Foundation.

1. Abrahams JP, Leslie AGW, Lutter R, Walker JE (1994) Structure at 2.8 Å resolution of F_1-ATPase from bovine heart mitochondria. *Nature* 370:621–628.
2. Foster DL, Fillingame RH (1982) Stoichiometry of subunits in the H^+-ATPase complex of *Escherichia coli*. *J Biol Chem* 257:2009–2015.
3. Junge W, Sielaff H, Engelbrecht S (2009) Torque generation and elastic power transmission in the rotary F_OF_1-ATPase. *Nature* 459:364–370.
4. Noji H, Yasuda R, Yoshida M, Kinosita K, Jr. (1997) Direct observation of the rotation of F_1-ATPase. *Nature* 386:299–302.
5. Boyer PD (1997) The ATP synthase—A splendid molecular machine. *Annu Rev Biochem* 66:717–749.
6. Yoshida M, Muneyuki E, Hisabori T (2001) ATP synthase—A marvellous rotary engine of the cell. *Nat Rev Mol Cell Biol* 2:669–677.
7. Dimroth P, von Ballmoos C, Meier T (2006) Catalytic and mechanical cycles in F-ATP synthases. Fourth in the Cycles Review Series. *EMBO Rep* 7:276–282.
8. McLachlin DT, Coveny AM, Clark SM, Dunn SD (2000) Site-directed cross-linking of b to the alpha, beta, and a subunits of the *Escherichia coli* ATP synthase. *J Biol Chem* 275: 17571–17577.
9. Vik SB, Ishmukhametov RR (2005) Structure and function of subunit a of the ATP synthase of *Escherichia coli*. *J Bioenerg Biomembr* 37:445–449.
10. Jones PC, Hermolin J, Jiang W, Fillingame RH (2000) Insights into the rotary catalytic mechanism of F_0F_1 ATP synthase from the cross-linking of subunits b and c in the *Escherichia coli* enzyme. *J Biol Chem* 275:31340–31346.
11. Del Rizzo PA, Bi Y, Dunn SD, Shilton BH (2002) The "second stalk" of *Escherichia coli* ATP synthase: Structure of the isolated dimerization domain. *Biochemistry* 41: 6875–6884.
12. Wächter A, et al. (2011) Two rotary motors in F-ATP synthase are elastically coupled by a flexible rotor and a stiff stator stalk. *Proc Natl Acad Sci USA* 108:3924–3929.
13. Schneider E, Altendorf K (1985) All three subunits are required for the reconstitution of an active proton channel (F_0) of *Escherichia coli* ATP synthase (F_1F_0). *EMBO J* 4: 515–518.
14. Wehrle F, Kaim G, Dimroth P (2002) Molecular mechanism of the ATP synthase's F_o motor probed by mutational analyses of subunit a. *J Mol Biol* 322:369–381.
15. Meier T, Polzer P, Diederichs K, Welte W, Dimroth P (2005) Structure of the rotor ring of F-type Na^+-ATPase from *Ilyobacter tartaricus*. *Science* 308:659–662.
16. Pogoryelov D, Yildiz Ö, Faraldo-Gómez JD, Meier T (2009) High-resolution structure of the rotor ring of a proton-dependent ATP synthase. *Nat Struct Mol Biol* 16:1068–1073.
17. Preiss L, Yildiz Ö, Hicks DB, Krulwich TA, Meier T (2010) A new type of proton coordination in an F_1F_o-ATP synthase rotor ring. *PLoS Biol* 8:e000443.
18. Murata T, Yamato I, Kakinuma Y, Leslie AG, Walker JE (2005) Structure of the rotor of the V-Type Na^+-ATPase from *Enterococcus hirae*. *Science* 308:654–659.
19. Symersky J, et al. (2012) Structure of the c_{10} ring of the yeast mitochondrial ATP synthase in the open conformation. *Nat Struct Mol Biol* 19:485–491.
20. Pogoryelov D, et al. (2010) Microscopic rotary mechanism of ion translocation in the F_o complex of ATP synthases. *Nat Chem Biol* 6:891–899.
21. Mizutani K, et al. (2011) Structure of the rotor ring modified with *N,N′*-dicyclohexylcarbodiimide of the Na^+-transporting vacuolar ATPase. *Proc Natl Acad Sci USA* 108:13474–13479.
22. Valiyaveetil FI, Fillingame RH (1998) Transmembrane topography of subunit a in the *Escherichia coli* F_1F_0 ATP synthase. *J Biol Chem* 273:16241–16247.
23. Cain BD (2000) Mutagenic analysis of the F_0 stator subunits. *J Bioenerg Biomembr* 32: 365–371.
24. Lightowlers RN, Howitt SM, Hatch L, Gibson F, Cox GB (1987) The proton pore in the Escherichia coli F_0F_1-ATPase: A requirement for arginine at position 210 of the a-subunit. *Biochim Biophys Acta* 894:399–406.

25. Mitome N, et al. (2010) Essential arginine residue of the F_o-a subunit in F_o-ATP synthase has a role to prevent the proton shortcut without c-ring rotation in the F_o proton channel. *Biochem J* 430:171–177.
26. Jiang W, Fillingame RH (1998) Interacting helical faces of subunits a and c in the F_1F_o ATP synthase of *Escherichia coli* defined by disulfide cross-linking. *Proc Natl Acad Sci USA* 95:6607–6612.
27. Vorburger T, et al. (2008) Arginine-induced conformational change in the c-ring/a-subunit interface of ATP synthase. *FEBS J* 275:2137–2150.
28. Steed PR, Fillingame RH (2009) Aqueous accessibility to the transmembrane regions of subunit c of the *Escherichia coli* F_1F_0 ATP synthase. *J Biol Chem* 284:23243–23250.
29. Angevine CM, Herold KA, Vincent OD, Fillingame RH (2007) Aqueous access pathways in ATP synthase subunit a. Reactivity of cysteine substituted into transmembrane helices 1, 3, and 5. *J Biol Chem* 282:9001–9007.
30. Lau WC, Rubinstein JL (2012) Subnanometre-resolution structure of the intact *Thermus thermophilus* H^+-driven ATP synthase. *Nature* 481:214–218.
31. Hoffmann J, et al. (2010) ATP synthases: Cellular nanomotors characterized by LILBID mass spectrometry. *Phys Chem Chem Phys* 12:13375–13382.
32. Meier T, et al. (2007) A tridecameric c ring of the adenosine triphosphate (ATP) synthase from the thermoalkaliphilic *Bacillus* sp. strain TA2.A1 facilitates ATP synthesis at low electrochemical proton potential. *Mol Microbiol* 65:1181–1192.
33. Stock D, Leslie AGW, Walker JE (1999) Molecular architecture of the rotary motor in ATP synthase. *Science* 286:1700–1705.
34. Stahlberg H, et al. (2001) Bacterial Na^+-ATP synthase has an undecameric rotor. *EMBO Rep* 2:229–233.
35. Vonck J, et al. (2002) Molecular architecture of the undecameric rotor of a bacterial Na^+-ATP synthase. *J Mol Biol* 321:307–316.
36. Meier T, et al. (2003) Evidence for structural integrity in the undecameric c-rings isolated from sodium ATP synthases. *J Mol Biol* 325:389–397.
37. Meier T, Matthey U, Henzen F, Dimroth P, Müller DJ (2001) The central plug in the reconstituted undecameric c cylinder of a bacterial ATP synthase consists of phospholipids. *FEBS Lett* 505:353–356.
38. Meier T, et al. (2005) Structural evidence for a constant c_{11} ring stoichiometry in the sodium F-ATP synthase. *FEBS J* 272:5474–5483.
39. van Heel M, Harauz G, Orlova EV, Schmidt R, Schatz M (1996) A new generation of the IMAGIC image processing system. *J Struct Biol* 116:17–24.
40. Schwem BE, Fillingame RH (2006) Cross-linking between helices within subunit a of *Escherichia coli* ATP synthase defines the transmembrane packing of a four-helix bundle. *J Biol Chem* 281:37861–37867.
41. Moore KJ, Fillingame RH (2008) Structural interactions between transmembrane helices 4 and 5 of subunit a and the subunit c ring of *Escherichia coli* ATP synthase. *J Biol Chem* 283:31726–31735.
42. Stouffer AL, et al. (2008) Structural basis for the function and inhibition of an influenza virus proton channel. *Nature* 451:596–599.
43. Gonzales EB, Kawate T, Gouaux E (2009) Pore architecture and ion sites in acid-sensing ion channels and P2X receptors. *Nature* 460:599–604.
44. Matthies D, et al. (2009) The c_{13} ring from a thermoalkaliphilic ATP synthase reveals an extended diameter due to a special structural region. *J Mol Biol* 388:611–618.
45. Gipson B, Zeng X, Zhang ZY, Stahlberg H (2007) 2dx–user-friendly image processing for 2D crystals. *J Struct Biol* 157:64–72.
46. Henderson R, Baldwin JM, Downing KH, Lepault J, Zemlin F (1986) Structure of purple membrane from *Halobacterium halobium*: Recording, measurement and evaluation of electron micrographs at 3.5 Å resolution. *Ultramicroscopy* 19:147–178.
47. Collaborative Computational Project, N. (1994) The CCP4 Suite: Programs for Protein Crystallography *Acta Crystallogr D Biol Crystallogr* 50:760–763.